PNAS RESEARCH ARTICLE | CHEMISTRY

In situ optical spectroscopy of crystallization: One crystal nucleation at a time

Oscar Urquidi[a,1], Johanna Brazard[a,1], Natalie LeMessurier[b], Lena Simine[b], and Takuji B. M. Adachi[a,2]

Edited by Pablo Debenedetti, Princeton University, Princeton, NJ; received December 22, 2021; accepted March 3, 2022

While crystallization is a ubiquitous and an important process, the microscopic picture of crystal nucleation is yet to be established. Recent studies suggest that the nucleation process can be more complex than the view offered by the classical nucleation theory. Here, we implement single crystal nucleation spectroscopy (SCNS) by combining Raman microspectroscopy and optical trapping induced crystallization to spectroscopically investigate one crystal nucleation at a time. Raman spectral evolution during a single glycine crystal nucleation from water, measured by SCNS and analyzed by a nonsupervised spectral decomposition technique, uncovered the Raman spectrum of prenucleation aggregates and their critical role as an intermediate species in the dynamics. The agreement between the spectral feature of prenucleation aggregates and our simulation suggests that their structural order emerges through the dynamic formation of linear hydrogen-bonded networks. The present work provides a strong impetus for accelerating the investigation of crystal nucleation by optical spectroscopy.

crystal nucleation | in situ Raman microspectroscopy | optical trapping induced crystallization | density functional calculation | molecular dynamics simulation

Significance

It is of fundamental importance to establish the microscopic picture of crystal nucleation for both academic and industrial research. Here, we report an in situ time-resolved Raman spectroscopy to study crystallization from solution, one crystal nucleation at a time. The observed dynamics of α-glycine crystallization from water without any additive supports the nonclassical nucleation pathway, where prenucleation aggregates form and convert to a crystal. By the direct comparison of Raman spectrum of the aggregates between the experiment and simulation, we propose the structure of these aggregates as linear hydrogen-bonded networks. We demonstrate the power of studying one nucleation event at a time, which can accelerate the investigation of crystal nucleation by optical spectroscopy.

Crystallization is a key process in a wide range of disciplines from fundamental science to industrial application (1–3). Despite the importance of controlling the crystallization and its morphology (e.g., polymorphism), the lack of microscopic description of crystal nucleation limits the rational approach to its engineering and control (2). A major challenge in establishing the molecular level understanding of crystal nucleation is its stochastic and heterogeneous nature at the nanoscale (1). This has long prevented experimentalists from directly observing the nucleation event in real time. Statistical approaches, such as determining the nucleation rate under various crystallization conditions, have been the major experimental methods to circumvent the difficulty (1, 4). The discrepancy between the nucleation rate obtained from the statistical experiments and the one predicted by classical nucleation theory (CNT) has led to a general agreement that crystal nucleation may be a more complex phenomenon than how it is described by CNT (4–7).

A real-time observation of nucleation dynamics has been long desired as a critical step in establishing its microscopic picture. For example, crystallization of colloidal particles has been used as a model system to mimic the dynamics of crystallization because the assembly process of particles can be easily visualized in real-time by optical microscopy (8, 9). A recent breakthrough in tackling this problem was the development of cryo- and liquid cell transmission electron microscopy (TEM) for visualizing crystallization of atomic/molecular systems (10, 11). The presence of morphologically "featureless" or "amorphous" clusters was confirmed in these TEM studies (12, 13), and in situ TEM results caught the moment at which clusters became well-defined crystals (14, 15). Further discussions are being held whether these observations can be simply generalized to the crystallization in bulk solution due to the specific crystallization condition of TEM experiments (10). Yet, more and more studies show the involvement of prenucleation aggregates in crystal nucleation process and suggest the complexity of crystal nucleation process in contrast to CNT (5–7, 12, 14, 16). While the debate continues whether crystal nucleation occurs through classical or nonclassical nucleation mechanism, the next critical steps toward establishing a microscopic picture include the detailed understanding of the structure of prenucleation aggregates (crystalline order under CNT, amorphous or possibly some degree of structural order under nonclassical mechanism) and how the crystalline order emerges from them if the nucleation proceeds by nonclassical mechanism (17, 18).

Optical spectroscopy could be a powerful technique to extract the molecular level details of the structure of prenucleation aggregates and their structural dynamics toward the phase transition. The application of optical spectroscopy on crystal nucleation problem has been, however, limited because the stochastic and heterogeneous nature of the nucleation process is detrimental to the interpretation of the spectroscopic signals. If one probes a large volume of a sample to capture a nucleation event that can occur

Author affiliations: [a]Department of Physical Chemistry, Sciences II, University of Geneva, 1211 Geneva, Switzerland; and [b]Department of Chemistry, McGill University, Montreal, QC H3A 0B8, Canada

Author contributions: T.B.M.A. designed research; O.U., J.B., N.L., L.S., and T.B.M.A. performed research; J.B. contributed new reagents/analytic tools; O.U., J.B., N.L., L.S., and T.B.M.A. analyzed data; and O.U., J.B., N.L., L.S., and T.B.M.A. wrote the paper.

The authors declare no competing interest.

This article is a PNAS Direct Submission.

See online for related content such as Commentaries.

[1]O.U. and J.B. contributed equally to this work.

[2]To whom correspondence may be addressed. Email: Takuji.Adachi@unige.ch.

This article contains supporting information online at http://www.pnas.org/lookup/suppl/doi:10.1073/pnas.2122990119/-/DCSupplemental.

Published April 8, 2022.

anywhere at any time, the obtained spectroscopic signal is obscured by the average of various species in solution (e.g., monomers, aggregates, and crystals). Although not applied in this field yet, there is a well-established powerful concept to deal with a stochastic, complex, and heterogenous system: single-molecule spectroscopy (19). The key to bring optical spectroscopy with its full potential to the field of crystallization is to probe one nucleation event at a time, which is only possible if one can predict precisely where a nucleation occurs.

Herein, we report the demonstration of single crystal nucleation spectroscopy (SCNS) which spectroscopically probes crystallization dynamics in aqueous solution one crystal nucleation at a time. SCNS is based on an extension of optical trapping Raman microspectroscopy, a well-established tool to study a trapped single object (20–22). Raman spectroscopy is a powerful tool that has been used to follow crystal polymorph conversion (23) and probe the formation of semiordered solution during a secondary (contact) nucleation (24). In SCNS, optical trapping is used to confine a crystal nucleation event within a focused laser spot instead of as a tweezer to trap an object. Optical trapping-induced crystallization (OTIC) was first demonstrated by Sugiyama et al. (25) in 2007 by focusing a near-infrared (NIR) laser in supersaturated glycine/D_2O solution. When a laser beam is tightly focused in solution, optical gradient force attracts particles toward the focus spot [cf. optical trapping in Rayleigh regime described by Ashkin et al. (26) and Harada et al. (27)]. Optical gradient force is, however, not large enough to trap a single molecule, and therefore it is generally assumed that the crystallization occurs as a result of local concentration increase by trapping aggregates in solution. Since its discovery, OTIC has been applied to a variety of systems (28–30), and furthermore high-quality single crystals can be prepared while the polymorphs can be chosen by laser polarization (30, 31). Our approach applies OTIC to spatially control a single crystal nucleation event (i.e., at a focused laser spot), so that a probe beam can be placed at the same position to track the nucleation process. We achieved measuring Raman spectral evolution of glycine crystal formation from water with 46-ms time resolution at room temperature. The fast spectral acquisition allowed us to extract the Raman spectrum of prenucleation aggregates and its kinetics during a nucleation. The comparison between the experimental and simulated Raman spectra of glycine aggregates provided new insights into the glycine crystallization dynamics such as the dynamic formation of linear hydrogen-bonded networks at the prenucleation stage.

Results and Discussion

The in situ SCNS setup to track single crystal nucleation dynamics was custom built based on an inverted microscope (Fig. 1*A*). While OTIC has been performed using a NIR laser in the past (25, 28–31), we used a 532-nm continuous-wave (CW) laser that served the dual role of inducing a crystal nucleation and Raman excitation (Fig. 1*B*). This design has two major benefits: 1) the setup is as simple as conventional confocal microscope and 2) high laser power (>1 W at the sample) required to induce crystallization produces high Raman signal (cf. typical Raman spectroscopy is performed using ∼10 mW with seconds to minutes accumulation time), which increases the temporal resolution of Raman spectroscopy (46 ms in this report). The other benefits of a 532-nm laser compared with an NIR laser is that Raman scattering is more efficient and the temperature of water at laser focus does not increase (estimated as ∼20 mK W^{-1}) (32, 33). The polarization of the laser beam was randomized by a depolarizer to minimize any laser polarization effect on crystallization process, to mimic a "natural" crystallization occurring in solution. It is important to note that a focused CW green laser does not induce crystal nucleation immediately upon the laser irradiation. In fact, the time from the beginning of laser irradiation until crystallization event varies from minutes to an hour, which indicates that crystallization still occurs stochastically as in regular crystallization. This is contrary to the report of laser induced crystallization by pulsed lasers where even one pulse can cause crystal nucleation (34–36). This is because the fluence of pulsed lasers is multiple order of magnitude higher than a focused CW laser. Additionally, we have never observed the formation of γ-glycine crystal in the 112 performed experiments with a depolarized focused CW beam, while γ-glycine crystal was formed by linearly polarized pulsed lasers (34) or linearly/circularly polarized CW lasers (31). The use of the depolarized beam also simplified the interpretation of Raman spectroscopy by eliminating Raman spectral variation due to polarization selection rules.

Glycine crystallization from water was chosen as a model system in this study. While glycine has been widely studied as it is the simplest amino acid, its crystallization process is complex and has been under active debates (37–44). The major hypothesis has been that α-glycine forms in water as a result of the assembly of doubly hydrogen-bonded cyclic dimers in a highly concentrated glycine solution (37). Molecular dynamics simulations on glycine aqueous solutions have shown that glycine molecules do not form the doubly hydrogen-bonded cyclic dimers but instead form clusters mediated by the hydrogen bonding (40, 42). Recent studies based on X-ray diffraction, solid-state NMR, and cryo-TEM on flash cooled glycine aqueous solution proposed a new hypothesis that α-glycine crystallization occurs via glycine dihydrates and β-glycine (41, 43, 45). While the formation of β-glycine from water was observed at room temperature for example in nanopores (46, 47), the presence of glycine dihydrates has not yet been confirmed at room temperature.

SCNS on glycine crystallization was performed by focusing a depolarized beam (1.2 W) in the glycine aqueous solution (the degree of supersaturation [SS] = 1.2). Fig. 1 *C–H* shows a series of Raman spectra obtained in situ during a single crystal nucleation of glycine, which highlights the dynamic nature of crystal nucleation (Movie S1). Over the course of a nucleation, broad Raman bands around 3,200 to 3,500 cm^{-1} due to O-H vibration of water molecules decreased. This coincides with the appearance of a small blurry object in the bright field image, starting from the frame shown in Fig. 1*D*. These observations can be interpreted as the local concentration of glycine molecules increased and pushed water molecules out of the confocal detection volume. The formation of a crystal is clearly captured with the increase of Raman intensity and the appearance of new peaks (Fig. 1*E*), even if the bright field image remains blurry. Among various spectral changes upon nucleation, the appearance of the Raman peak at 2,955 cm^{-1} caught our immediate attention because α-glycine (C-H stretching mode: ∼2,970 cm^{-1}) was expected to form in water. From the comparison of features with the reference spectra of α-, β- and γ-glycine measured on the same setup (*SI Appendix*, Fig. S1), the species was identified as β-glycine. The Raman spectral feature of β-glycine was short-lived and quickly became that of α-glycine (Fig. 1 *F* and *G*).

The spectral evolution during a glycine nucleation was analyzed using nonnegative matrix factorization (NMF), a type of unsupervised principal component analysis used in machine

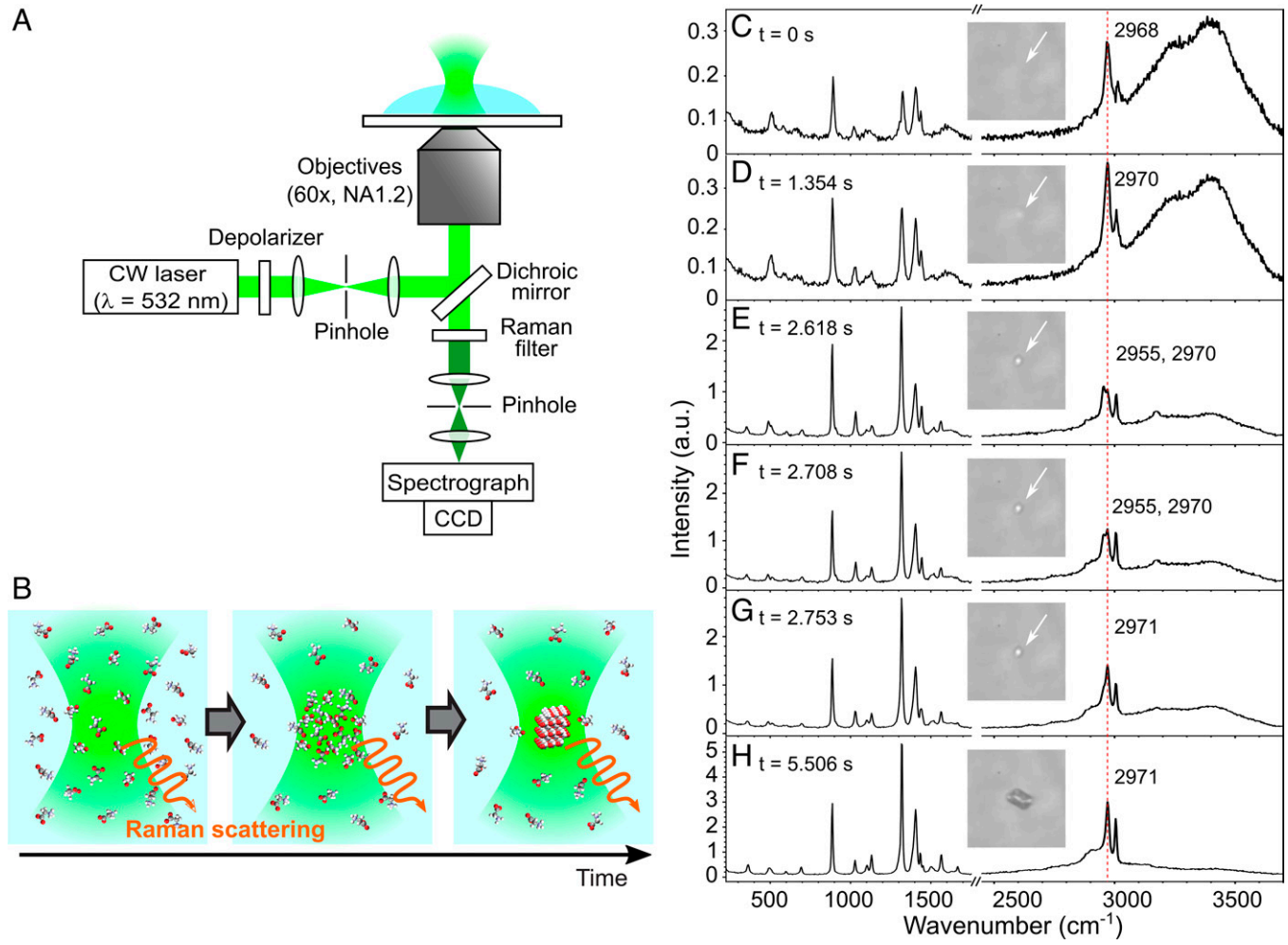

Fig. 1. SCNS: In situ Raman spectroscopy during α-glycine crystallization one crystal nucleation at a time. (*A*) A simple scheme of the home-built SCNS setup to achieve in situ Raman measurement during single crystal nucleation. (*B*) A cartoon representing the dual role of 532 nm CW laser. Crystallization occurs from a focused CW laser spot while the laser also serves as the excitation source for Raman scattering to track the crystallization dynamics. (*C*–*H*) Snapshots (46-ms time resolution) of Raman spectral evolution during α-glycine crystallization. Time 0 is set as the beginning of the nucleation process which is 2.5 min after the laser irradiation was started. Insets are the bright field microscopy images (16 × 16 μm) taken at the corresponding time to each acquired spectrum.

learning analysis (Fig. 2) (48). NMF has been used to deconvolute spectra in the field of Raman spectroscopy. A powerful aspect of this analysis algorithm is that a set of partial Raman spectrum (PRS), as well as the amplitude of each PRS during the spectral evolution, can be obtained without any assumption concerning the spectral shapes. The number of PRS used for the deconvolution is the only predetermined parameter. The analysis was performed on the spectral series in which clear features of β-glycine were observed for several seconds before converting to α-glycine, to minimize the complexity of the crystallization dynamics (*SI Appendix* for details). We first applied NMF analysis with two PRS to the spectral series (Fig. 2*A*), but it did not reach good fitting results (*SI Appendix*, Fig. S3). This indicates that the glycine crystal nucleation does not occur through CNT mechanism, where the whole spectral evolution should be reproduced by a linear combination of the spectrum of solution and crystal. Instead, good quality fit was achieved with three PRS (Fig. 2 *B*–*F*). One of the PRS (PRS-2) matches well with the Raman spectrum of β-glycine. Interestingly, the spectra before the appearance of β-glycine were deconvoluted to two PRS (PRS-1 and -3). PRS-1 resembled the spectrum of glycine aqueous solution at SS = 1.2. PRS-3, however, did not match any other reported spectrum including glycine dihydrates (45), another possible form of crystalline phase that was previously reported.

The temporal evolution of each PRS amplitude (Fig. 2*G*) captured remarkable dynamics of crystallization. Initially, the spectra were composed of 80 to 85% of PRS-1, 0% of PRS-2, and 15 to 20% of PRS-3. Just before the nucleation occurred at ∼2.65 s (corresponding to the sudden increase of the amplitude of PRS-2), the amplitude of PRS-1 decreased while that of PRS-3 increased (highlighted by gray color in Fig. 2*G*). Once a crystal formed, the amplitude of PRS-3 dropped down to almost zero. PRS-1 does not go down to zero at this time range, because there is still solution remaining in the focal volume, as the size of a crystal is still too small to occupy the whole focal volume (estimated as 0.52 μm^3). These dynamics were reproduced qualitatively in 33 experiments where three components were necessary and sufficient in the NMF, although there are some variances between the experiments due to the stochastic nature of crystallization (*SI Appendix*, Figs. S4 and S5 for more examples). These dynamics fit the description of the nonclassical nucleation model, therefore PRS-3 may be interpreted as the Raman spectrum of prenucleation aggregates.

It is worth noting that the amplitude of PRS-3 was steadily 15 to 20% before the nucleation event. This could mean that

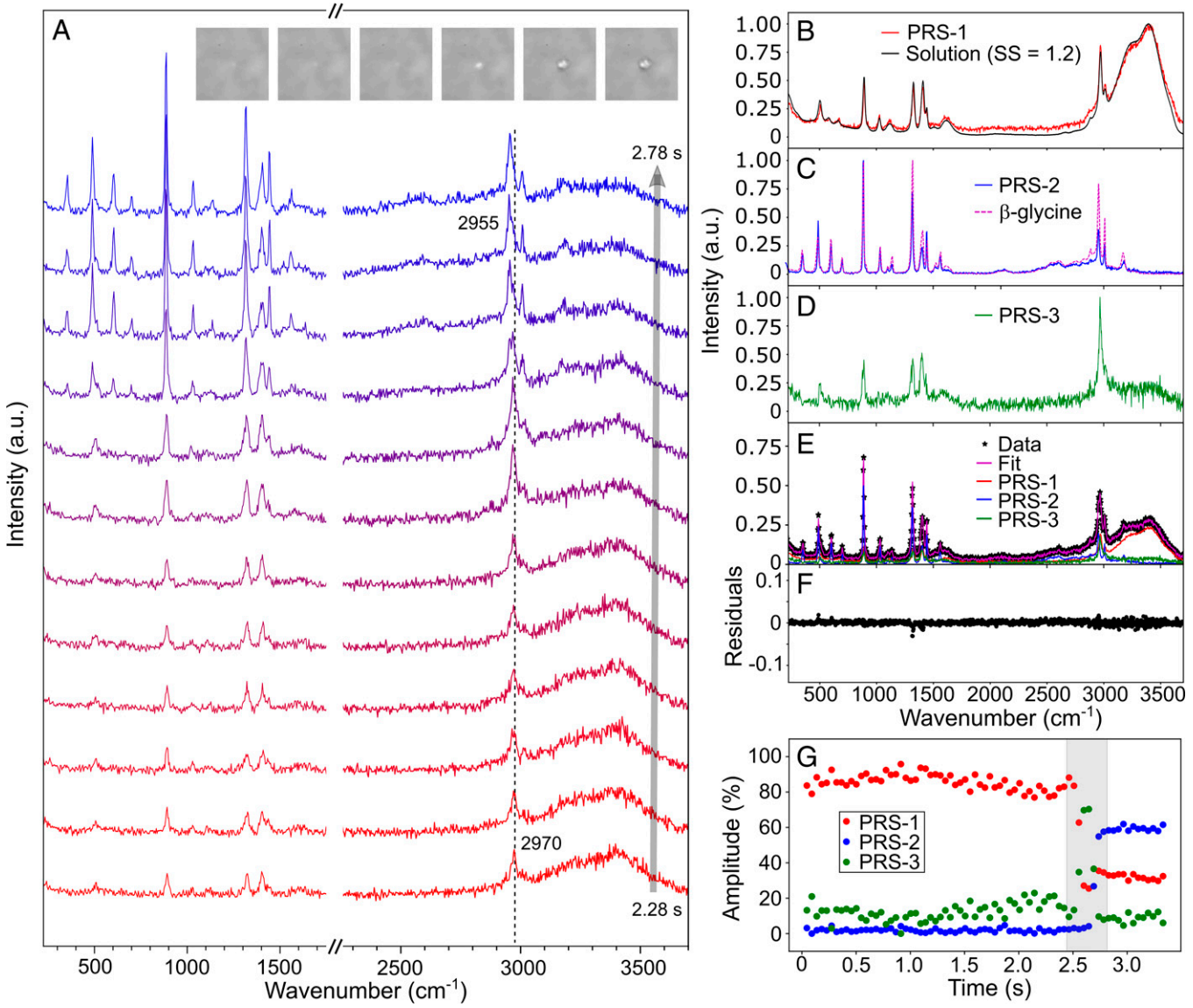

Fig. 2. Raman spectral evolution during a β-glycine crystal nucleation and its nonsupervised data decomposition analysis. (*A*) Snapshots of Raman spectra showing the phase transition from solution (bottom) to crystal (top) with the bright field microscopy images (16 × 16 μm) corresponding to every other spectrum (at 2.28 s to 2.78 s from the left to right) as *Insets*. Note: time 0 does not correspond to the beginning of the experiment but the spectral range used for the analysis. (*B–D*) Three spectra obtained by nonsupervised data decomposition of the series of spectra in the panel *A* (PRS-1 to -3) with reference spectra. (*E*) An example of the fit to the data (the frame at 2.69 s) by three constituents and (*F*) the residuals of the fit. (*G*) Temporal evolution of each constituent amplitude during the crystal nucleation.

the aggregates of glycine molecules are abundant in a supersaturated aqueous solution. To test this hypothesis, we measured Raman spectrum of glycine aqueous solution as a function of concentration (Fig. 3*A* and *SI Appendix*, Fig. S7). To minimize an effect of optical trapping on the local concentration, a low laser power (50 mW) was used for this series of measurements. The intensity of Raman spectrum increased with the concentration, as expected. The intensity, however, did not increase proportionally as a function of the concentration but rather showed a saturation behavior (Fig. 3*B*). Already at the lower concentration range of SS = 0.05 to 0.2, the constant of proportionality of the Raman peak increase is not one. This suggests that the glycine solution at SS = 0.1 is not purely composed of monomers and the concentration of aggregates increases with higher SS, as seen by the saturation behavior of the peak intensities. NMF analysis with two PRS resulted in an excellent fit to the series of Raman spectra (*SI Appendix*, Fig. S8). Due to the nature of principal component analysis, PRS-1' resembles the spectrum of the lowest concentration of the data set fed into the algorithm. We applied the NMF analysis for different concentration regions (e.g., SS = 0.2 to 1.6, 0.4 to 1. 6, 0.1 to 1.2, etc.) and verified that PRS-1' depends on the spectrum with the lowest intensity. PRS-2' was, however, not affected by the choice of concentration range (*SI Appendix*, Fig. S9 and Fig. 3*D*). PRS-2' represents the spectral variation that occurs nonlinearly upon the increase of the glycine concentration. As the change is due to the concentration increase, we assign PRS-2' as the spectrum of aggregates. For the comparison with the SCNS results described earlier (Fig. 2), the NMF analysis was applied to the concentration range of SS = 1.2 to 1.6 to obtain PRS-1' and 2' (Fig. 3 *C* and *D*).

Notably, the PRS assigned as aggregates (PRS-2') from the concentration series matches the spectral features of PRS-3 obtained from β-crystal nucleation dynamics (Fig. 3*D*). The PRS-1 from Fig. 2*B* matches the PRS-1' obtained from the concentration series of SS = 1.2 to 1.6 (Fig. 3*C*). These

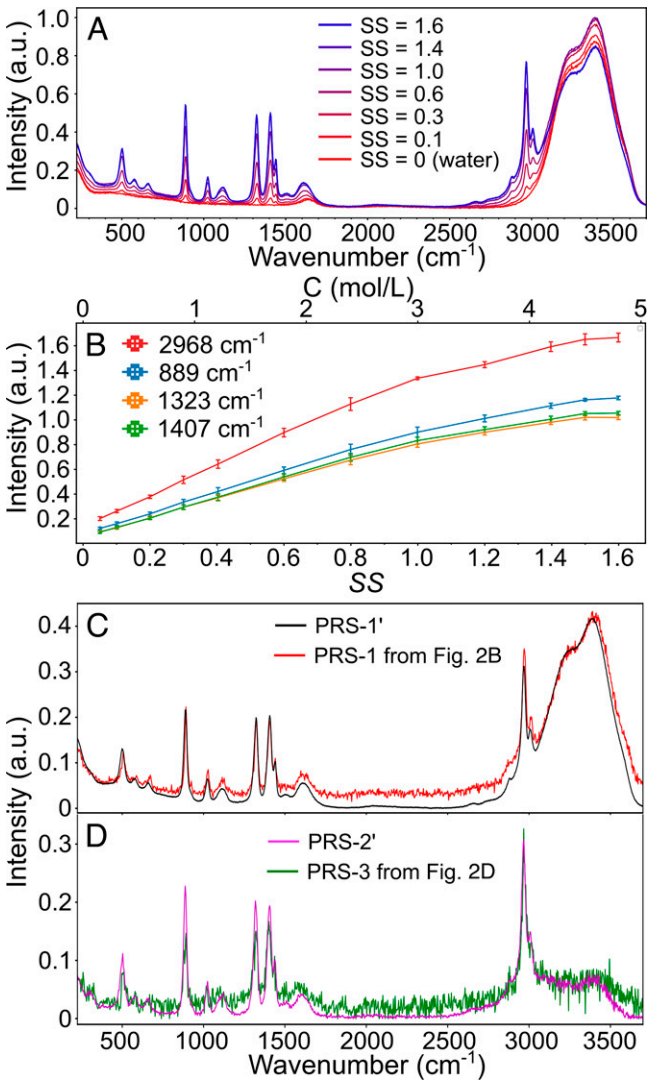

Fig. 3. A series of Raman spectra of glycine solution at different concentration and its NMF analysis revealing the spectrum of glycine monomers and aggregates. (*A*) Raman spectra of glycine solution at different concentration. (*B*) Raman peak intensity as a function of concentration at four positions. Error bars represent the SD from three measurements. (*C*) The overlay of PRS-1′ (obtained from NMF analysis of spectra at SS = 1.2 to 1.6) and PRS-1 obtained from the nucleation dynamics (Fig. 2*B*), and (*D*) PRS-2′ and PRS-3 (Fig. 2*D*).

comparisons support our interpretation of the observed nucleation dynamics (Fig. 2) discussed earlier. Crystal nucleation of glycine occurs in a nonclassical pathway, where prenucleation aggregates are formed and converted to a crystal. While there are always some aggregates present in solution and under the optical trapping laser, the amplitude of aggregates spectrum (PRS-3) increases toward crystal nucleation (Fig. 2*G* and *SI Appendix*, Figs. S4*G* and S5*G*). The increase of PRS-3 amplitude before the nucleation is likely due to the growth of the aggregate size upon the concentration increase. In this work, we could not estimate the size of aggregates prior to nucleation, because the Raman cross section of aggregates is not available to convert the amplitude of the PRS-1 and PRS-3 to the concentration ratio. Further experimental development based on SCNS platform, however, can be conceived to extract the size of nucleus by combining another spectroscopy tools.

Optical trapping favors the trapping of aggregates than monomers to locally increase the concentration, and therefore our results cannot completely exclude the possibility of classical nucleation mechanism of glycine crystallization from water in bulk solution. However, the fact glycine aggregates are readily present in solution (Fig. 3) leads us to an interesting question about the role of aggregates. For the crystal nucleation to occur through the classical mechanism in bulk solution, a crystalline-ordered nucleus must form through monomer-by-monomer attachment while "avoiding" these aggregates that simultaneously increase their amplitude as the concentration increases. We therefore propose that glycine crystallization in water occurs via the nonclassical mechanism, although there is still room for discussion.

While recent studies based on molecular dynamics simulation suggested that glycine molecules form large clusters through hydrogen bonding in aqueous solution (42, 49, 50), it has been challenging to experimentally test this hypothesis. In this work, we were determined to gain an insight into the structures of the prenucleation aggregates using the Raman spectrum of glycine aggregates as a link between the experiments and simulations. In our simulations, we aimed to qualitatively explore the prenucleation aggregation patterns of glycine (dimerization, trimerization, chain formation) in solution. It is worthwhile to note that the degree of supersaturation may differ in the simulation from experimental values and while the quantitative kinetics are known to sensitively depend on degree of supersaturation in the simulation (51–53) our qualitative discussion is not affected by this. To this end, we first ran molecular dynamics (MD) simulations using a polarizable force-field at two concentrations: 3.3 mol L^{-1} representing the initial concentration in the experiments and 5.2 mol L^{-1} modeling the effect of increasing concentration. We have analyzed the sampled configurations and performed density functional theory electronic structure calculations to obtain Raman spectra from glycine clusters of varying sizes (*Materials and Methods* and *SI Appendix* for the description of methods and technical details).

In order to learn about the configurations in which glycine tends to exist in solution based on our simulations, we analyzed the formation of clusters, identified their internal structure, and demonstrated the signature of the broad distribution of hydrogen bonding interactions in Raman spectra in our simulated structures. The size of glycine clusters in the MD simulation was analyzed by defining the clusters using a 2.5Å cutoff distance between any two atoms belonging to two different glycines. This cutoff value is just under the van der Waals distance between O–H in order to capture the thermal fluctuations in hydrogen bonding. Fig. 4*B* shows the histograms of the size of glycine clusters at two different concentrations. At the low concentration, monomers and open dimers dominate the solution. Doubly hydrogen-bonded cyclic dimers (37) were never observed in our simulations. We attribute this to the merits of the polarizable forcefields (AMOEBA was used) that capture the nuanced dynamics of a charged species in water. As the concentration increases, larger clusters emerge as seen in the histogram at the bottom of Fig. 4*B*. The insets show the characteristic outcomes of the network visualization analysis: red circles are individual glycines and the lines between them indicate contacts.

The internal structure of the glycine clusters was further analyzed by the connectivity analysis. In each snapshot in the high concentration (5.2 mol L^{-1}) trajectory, glycine residues involved in clusters with four or more members were identified; the average number of the nearest neighbors of these residues was computed and recorded, and then the collected data for the entire set of 2,000 frames in the trajectory were used to

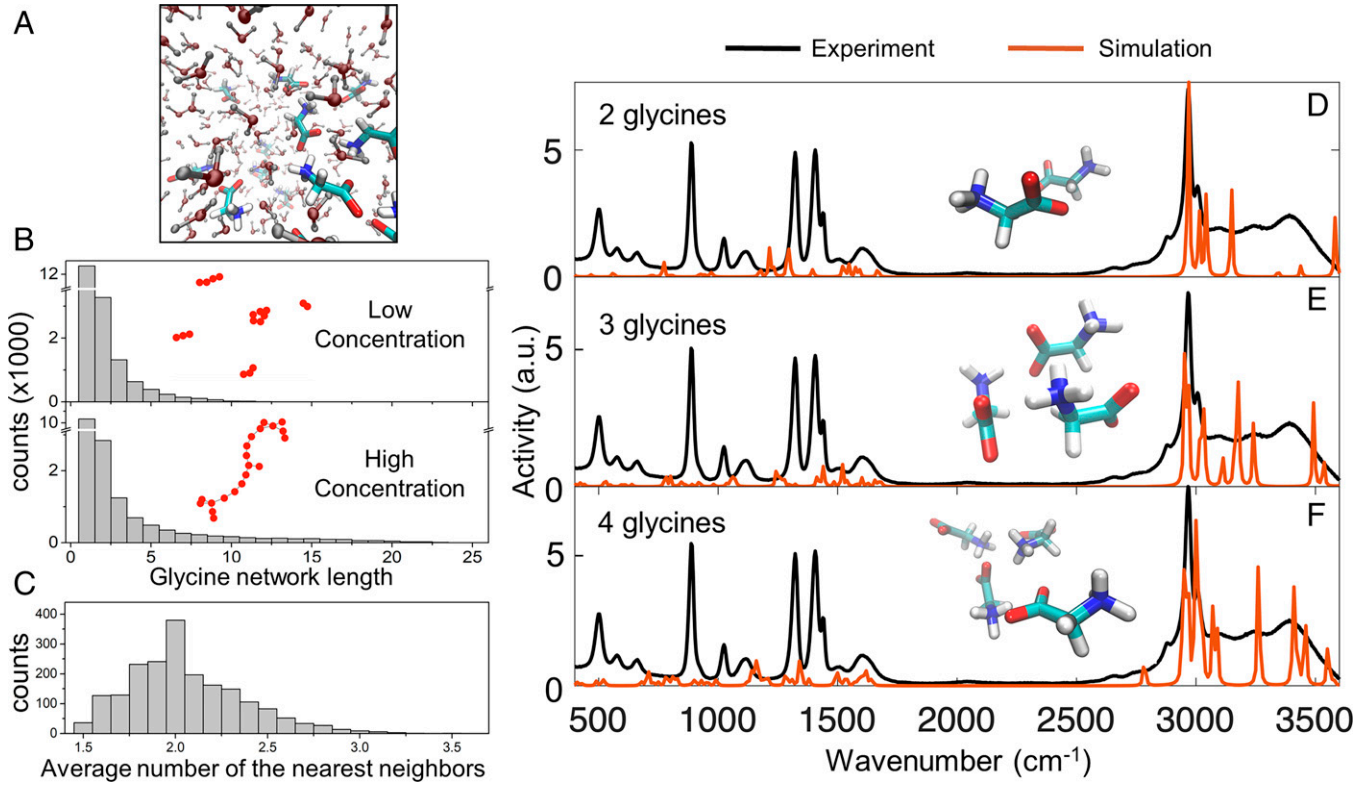

Fig. 4. MD simulation of glycine solutions and Raman spectrum calculations of glycine clusters. (*A*) A snapshot from a MD trajectory of glycines in water; (*B*) the effect of concentration on the formation of glycine-glycine contacts: at low concentration glycine predominantly exist as monomers and small clusters, and larger networks form in a linear fashion as the concentration increases. The insets are showing samples from the network visualizations: red circles are individual glycines, and the lines between them indicate contacts. Disconnected glycines are omitted. (*C*) The histogram of the average number of the nearest neighbors of glycine residues involved in the clusters that consist of more than four molecules. (*D–F*) (red) simulated Raman spectra from glycine clusters of increasing sizes sampled using MD: (*D*) two, (*E*) three, and (*F*) four glycines; the experimental PRS-2′ assigned to aggregates is shown in black.

construct the histogram shown in Fig. 4*C*. It was found that glycines had only 2.05 neighbors on average in large networks. This suggests that large aggregates of glycines in our simulations tend to be elongated chain-like structures. Glycine molecules in these linear networks tend to be oriented "head (NH_3^+)-to-tail (COO^-)" (Fig. 4*A* and *SI Appendix*, Fig. S10) and they curve up in the simulation box without collapsing into a homogeneous aggregate. The observed feature of glycine networks agrees with the previously reported hydrogen-bonded clusters of glycine, and we confirmed that the networks dynamically assemble and disassemble over time in agreement with the previous reports (40, 42).

The Raman spectral features indicate that there is a broad structural distribution of glycine linear networks that are held together by hydrogen-bonding interactions. The calculated Raman spectra for the clusters of two, three, four glycines (Fig. 4 *D–F*) show that the frequency of vibration can be shifted as a result of the intermolecular interactions. A broadening of Raman spectrum is resulting from the heterogeneity of the conformation of glycines in the hydrogen bonded clusters (Movies S2 and S3). As a result of heterogenous broadening, Raman peaks gradually "fill in" the broad spectroscopic feature observed in experiments (black), especially in the region of 3,000 to 3,500 cm^{-1} as the size of the clusters increases. This broad band in fact resembles the spectral feature of formamide (assigned as N–H–O band), which is known to form hydrogen-bonded linear networks (*SI Appendix*, Fig. S11) (54, 55). Collectively, we propose that the hydrogen-bonded networks observed in the simulations can be the common structural feature of prenucleation aggregate that are the precursors of β-glycine. Aggregates that are present in solution and prenucleation aggregates may be structurally similar (both hydrogen-bonded linear networks), but the latter is probably larger to reach the critical size of nucleation.

In summary, we demonstrated an in situ optical spectroscopy method to study crystallization dynamics of glycine one crystal nucleation at a time, which overcomes the difficultly imposed by stochastic and heterogeneous nature of the nucleation. Spectral dynamics obtained during single glycine nucleation events from aqueous solution at room temperature, along with nonsupervised spectral decomposition analysis, provided new evidence to understand the nucleation dynamics: 1) glycine crystallization occurs via nonclassical nucleation pathway, where prenucleation aggregates grow and nucleate and 2) the comparison between the experiments and simulations using the Raman spectrum of aggregates suggests that glycine molecules form linear hydrogen-bonded networks, which are the precursor to β-glycine crystal. An in situ spectroscopic approach presented in this study, SCNS, can be regarded as a basic platform to which more advanced spectroscopy techniques can be coupled. The present work identifies a modality for time-resolved study of crystal nucleation that provides a strong impetus for accelerating such investigations using additional capabilities of optical spectroscopy.

Materials and Methods

Sample Preparation. Glycine (Sigma-Aldrich) was used without further purification. Glycine aqueous solution was prepared using ultrapure water (MilliQ). Glycine was dissolved at 80 °C using ultrasonication, filtered with a 0.2 μm Target2 Nylon syringe filter (Thermo Scientific), and then slowly cooled down (~3 h) to room temperature in a dry bath (Thermo Scientific). The degree of SS was calculated using the solubility of glycine in water at 20 °C (0.225 g mL^{-1}) (56).

For SCNS, a sample was assembled by placing a silicone isolator sheet (0.25 mm thick; Grace Bio-Labs 664475) with a 10-mm hole on a piranha cleaned cover glass. The silicone sheet was cleaned in methanol before the use. Ten microliters of glycine aqueous solution (SS = 1.2) was dropped in the hole, which resulted in a thin film of glycine solution (100 μm thickness). Another cover glass was placed on top to prevent the evaporation of water. No spontaneous crystallization was observed for ∼1 h.

Conventional crystallization was performed to obtain α-, β-, and γ-glycine, to measure Raman spectrum of each phase (*SI Appendix*, Fig. S1). α-glycine was prepared by the slow evaporation of glycine aqueous solution. β-glycine was prepared by adding methanol to aqueous solution of glycine. γ-glycine was obtained by the slow evaporation of glycine aqueous solution with potassium nitrate as additive (*SI Appendix*).

SCNS Setup.

General scheme. The optical setup (Fig. 1*A*) was home-built based on an inverted microscope (Olympus IX73). A 532 nm CW laser (Laser Quantum, Opus 532) was used with a dual role for optical trapping and Raman excitation. The diameter of the laser beam was properly adjusted by a telescope to slightly overfill the back aperture of water-immersion objective lens (Olympus UPLSAPO60XW, NA1.2). Liquid crystal polymer depolarizer (Thorlabs, DPP25-A) was used to randomize the polarization of the laser beam. A periodic retardation pattern of the depolarizer generates two focus spots due to diffraction. The beam after the depolarizer was once focused by a lens to spatially filter one of the spots and then was recollimated (*SI Appendix*, Fig. S12). A dichroic beamsplitter (AHF analysentechnik AG, Raman beamsplitter RT 532 rdc, F78-535) and a 532 nm RazorEdge ultrasteep long-pass edge filter (Semrock, LP03-532RE-25) were used to remove the excitation beam from Raman scattering. The signal was spatially filtered at the conjugate plane using a 25 μm pinhole to remove the contribution of extrafocal volume. The size of the pinhole adopted in this setup is smaller than the one in typical setups (∼100 μm). Therefore, the contribution of Raman signal from the extrafocal volume is significantly reduced and the spectral sensitivity to the nucleation dynamics occurring at the laser focus is improved (57). The confocal volume (V_{eff}) with 25 μm pinhole was characterized as 0.52 μm^3 using fluorescence correlation spectroscopy (*SI Appendix*, Fig. S13). Raman spectrum was recorded by using a spectrograph (Andor, Kymera 193) and a CCD (Andor, iDus420) with a 900 l/mm density diffraction grating, blazed at 550 nm (Quantum Design AG, A-SR2-GRT-0900-0550).

Technical details of in situ glycine crystallization. The depolarized laser beam was focused just below (∼1 μm) the liquid–air interface of glycine solution. While it has been reported that the height of the liquid–air interface continuously changes during OTIC with a 1,064 nm laser (58), almost no change of the height was observed in the experiments with a 532 nm laser. This could simply be because there is no heating at the focus when 532 nm is used. OTIC with a 532 nm laser not only allows one to use aqueous solution instead of deuterated (D_2O) solution, but also reduces complications related with heat-induced flows around the focus spot. Although the height of the liquid–air interface was stable, we also verified that the spectral shape near the liquid–air interface does not change due to the focus position relative to the interface (*SI Appendix*, Fig. S14). When the beam is focused at or above the interface, Raman signal is lower because half or more of the focal volume probes air. Besides the intensity, the spectral shape remained unchanged.

Data Analysis. The raw data were noise-filtered by singular value decomposition (*SI Appendix*, Fig. S2). The cleaned spectra were analyzed by nonnegative matrix factorization (NMF) using the Scikit_Learn library in Python (59). For more details, see the *SI Appendix*.

Computational Simulations. Molecular dynamics simulations were run on the zwitterionic form of glycine in an 8 nm^3 water box using the AMOEBA 2013 forcefield (60) implemented in the OpenMM toolkit (61) at two concentrations: 3.3 mol L^{-1} and 5.2 mol L^{-1}. The Raman spectra calculations were performed on clusters obtained from the MD trajectories using the Gaussian 16 suite of programs (62) with B3LYP/6-311G(d) (39). For the complete technical discussion, see *SI Appendix*, Section S2.

Data Availability. Python codes and data that support the findings of this study are available in Yareta (DOI: 10.26037/yareta:gll2fuxk6fanhkzfw76beqeqwq)

ACKNOWLEDGMENTS. T.B.M.A., O.U., and J.B. are thankful for the financial support from the University of Geneva. Computations were made on the supercomputer Béluga, managed by Calcul Québec (https://www.calculquebec.ca/) and Compute Canada (https://www.computecanada.ca/). The operation of this supercomputer is funded by the Canada Foundation for Innovation (CFI).

1. J. W. Mullin, *Crystallization* (Elsevier Science, 2014).
2. J. Bernstein, *Polymorphism in Molecular Crystals* (Oxford University Press, 2002).
3. R. Tamura, M. Miyata, *Advances in Organic Crystal Chemistry Comprehensive Reviews 2015* (Springer, 2015).
4. G. C. Sosso *et al.*, Crystal nucleation in liquids: Open questions and future challenges in molecular dynamics simulations. *Chem. Rev.* **116**, 7078–7116 (2016).
5. D. Erdemir, A. Y. Lee, A. S. Myerson, Nucleation of crystals from solution: Classical and two-step models. *Acc. Chem. Res.* **42**, 621–629 (2009).
6. D. Gebauer, M. Kellermeier, J. D. Gale, L. Bergström, H. Cölfen, Pre-nucleation clusters as solute precursors in crystallisation. *Chem. Soc. Rev.* **43**, 2348–2371 (2014).
7. M. Jehannin, A. Rao, H. Cölfen, New horizons of nonclassical crystallization. *J. Am. Chem. Soc.* **141**, 10120–10136 (2019).
8. P. Schall, I. Cohen, D. A. Weitz, F. Spaepen, Visualizing dislocation nucleation by indenting colloidal crystals. *Nature* **440**, 319–323 (2006).
9. F. Dong, M. Liu, V. Grebe, M. D. Ward, M. Weck, Assembly of shape-tunable colloidal dimers in a dielectrophoretic field. *Chem. Mater.* **32**, 6898–6905 (2020).
10. J. J. De Yoreo, N. A. J. M. Sommerdijk, Investigating materials formation with liquid-phase and cryogenic TEM. *Nat. Rev. Mater.* **1**, 16035 (2016).
11. F. M. Ross, Opportunities and challenges in liquid cell electron microscopy. *Science* **350**, aaa9886 (2015).
12. Y. Tsarfati *et al.*, Crystallization of organic molecules: Nonclassical mechanism revealed by direct imaging. *ACS Cent. Sci.* **4**, 1031–1036 (2018).
13. R. E. Schreiber *et al.*, Real-time molecular scale observation of crystal formation. *Nat. Chem.* **9**, 369–373 (2017).
14. T. Yamazaki *et al.*, Two types of amorphous protein particles facilitate crystal nucleation. *Proc. Natl. Acad. Sci. U.S.A.* **114**, 2154–2159 (2017).
15. T. Nakamuro, M. Sakakibara, H. Nada, K. Harano, E. Nakamura, Capturing the moment of emergence of crystal nucleus from disorder. *J. Am. Chem. Soc.* **143**, 1763–1767 (2021).
16. P. G. Vekilov, The two-step mechanism of nucleation of crystals in solution. *Nanoscale* **2**, 2346–2357 (2010).
17. R. J. Davey, S. L. M. Schroeder, J. H. ter Horst, Nucleation of organic crystals–A molecular perspective. *Angew. Chem. Int. Ed. Engl.* **52**, 2166–2179 (2013).
18. S. Price *et al.*, Molecular self-assembly and clustering in nucleation processes: General discussion. *Faraday Discuss.* **179**, 155–197 (2015).
19. P. F. Barbara, Single-molecule spectroscopy. *Acc. Chem. Res.* **38**, 503 (2005).
20. J. Buajarern, L. Mitchem, J. P. Reid, Manipulation and characterization of aqueous sodium dodecyl sulfate/sodium chloride aerosol particles. *J. Phys. Chem. A* **111**, 13038–13045 (2007).
21. J. W. Chan, Recent advances in laser tweezers Raman spectroscopy (LTRS) for label-free analysis of single cells. *J. Biophotonics* **6**, 36–48 (2013).
22. R. Mrad, S. G. Kruglik, N. Ben Brahim, R. Ben Chaâbane, M. Negrerie, Raman tweezers microspectroscopy of functionalized 4.2 nm diameter CdSe nanocrystals in water reveals changed ligand vibrational modes by a metal cation. *J. Phys. Chem. C* **123**, 24912–24918 (2019).
23. X. Yang, J. Lu, X. Wang, C. B. Ching, *In situ* monitoring of the solution-mediated polymorphic transformation of glycine: Characterization of the polymorphs and observation of the transformation rate using Raman spectroscopy and microscopy. *J. Raman Spectrosc.* **39**, 1433–1439 (2008).
24. P. Elankovan, K. A. Berglund, Technique for obtaining Raman spectra of contact nuclei *in situ*. *Appl. Spectrosc.* **40**, 712–714 (1986).
25. T. Sugiyama, T. Adachi, H. Masuhara, Crystallization of glycine by photon pressure of a focused CW laser beam. *Chem. Lett.* **36**, 1480–1481 (2007).
26. A. Ashkin, J. M. Dziedzic, J. E. Bjorkholm, S. Chu, Observation of a single-beam gradient force optical trap for dielectric particles. *Opt. Lett.* **11**, 288 (1986).
27. Y. Harada, T. Asakura, Radiation forces on a dielectric sphere in the Rayleigh scattering regime. *Opt. Commun.* **124**, 529–541 (1996).
28. K. I. Yuyama, M. J. Islam, K. Takahashi, T. Nakamura, V. Biju, Crystallization of methylammonium lead halide perovskites by optical trapping. *Angew. Chem. Int. Ed. Engl.* **57**, 13424–13428 (2018).
29. A.-C. Cheng, H. Masuhara, T. Sugiyama, Evolving crystal morphology of potassium chloride controlled by optical trapping. *J. Phys. Chem. C* **124**, 6913–6921 (2020).
30. T. Sugiyama, K. Yuyama, H. Masuhara, Laser trapping chemistry: From polymer assembly to amino acid crystallization. *Acc. Chem. Res.* **45**, 1946–1954 (2012).
31. K. Yuyama, T. Rungsimanon, T. Sugiyama, H. Masuhara, Selective fabrication of α- and γ-polymorphs of glycine by intense polarized continuous wave laser beams. *Cryst. Growth Des.* **12**, 2427–2434 (2012).
32. S. Ito, T. Sugiyama, N. Toitani, G. Katayama, H. Miyasaka, Application of fluorescence correlation spectroscopy to the measurement of local temperature in solutions under optical trapping condition. *J. Phys. Chem. B* **111**, 2365–2371 (2007).
33. G. M. Hale, M. R. Querry, Optical constants of water in the 200-nm to 200-microm wavelength region. *Appl. Opt.* **12**, 555–563 (1973).
34. B. A. Garetz, J. E. Aber, N. L. Goddard, R. G. Young, A. S. Myerson, Nonphotochemical, polarization-dependent, laser-induced nucleation in supersaturated aqueous urea solutions. *Phys. Rev. Lett.* **77**, 3475–3476 (1996).
35. B. Clair *et al.*, A new experimental setup for high-throughput controlled non-photochemical laser-induced nucleation: Application to glycine crystallization. *J. Appl. Cryst.* **47**, 1252–1260 (2014).

36. A. J. Alexander, P. J. Camp, Non-photochemical laser-induced nucleation. *J. Chem. Phys.* **150**, 040901 (2019).
37. I. Weissbuch, V. Yu. Torbeev, L. Leiserowitz, M. Lahav, Solvent effect on crystal polymorphism: Why addition of methanol or ethanol to aqueous solutions induces the precipitation of the least stable β form of glycine. *Angew. Chem. Int. Ed. Engl.* **44**, 3226–3229 (2005).
38. J. Huang, T. C. Stringfellow, L. Yu, Glycine exists mainly as monomers, not dimers, in supersaturated aqueous solutions: Implications for understanding its crystallization and polymorphism. *J. Am. Chem. Soc.* **130**, 13973–13980 (2008).
39. P. Friant-Michel, M. F. Ruiz-López, Glycine dimers: Structure, stability, and medium effects. *ChemPhysChem* **11**, 3499–3504 (2010).
40. Y. Yani, P. S. Chow, R. B. H. Tan, Glycine open dimers in solution: New insights into α-glycine nucleation and growth. *Cryst. Growth Des.* **12**, 4771–4778 (2012).
41. W. Xu, Q. Zhu, C. T. Hu, The structure of glycine dihydrate: Implications for the crystallization of glycine from solution and its structure in outer space. *Angew. Chem. Int. Ed. Engl.* **56**, 2030–2034 (2017).
42. Y. G. Bushuev, S. V. Davletbaeva, O. I. Koifman, Molecular dynamics simulations of aqueous glycine solutions. *CrystEngComm* **19**, 7197–7206 (2017).
43. P. Cerreia Vioglio *et al.*, Insights into the crystallization and structural evolution of glycine dihydrate by in situ solid-state NMR spectroscopy. *Angew. Chem. Int. Ed. Engl.* **57**, 6619–6623 (2018).
44. E. T. Broadhurst *et al.*, Polymorph evolution during crystal growth studied by 3D electron diffraction. *IUCrJ* **7**, 5–9 (2020).
45. N. V. Surovtsev *et al.*, Glycine phases formed from frozen aqueous solutions: Revisited. *J. Chem. Phys.* **137**, 065103 (2012).
46. Q. Jiang, C. Hu, M. D. Ward, Stereochemical control of polymorph transitions in nanoscale reactors. *J. Am. Chem. Soc.* **135**, 2144–2147 (2013).
47. M. Juramy *et al.*, Monitoring crystallization processes in confined porous materials by dynamic nuclear polarization solid-state nuclear magnetic resonance. *J. Am. Chem. Soc.* **143**, 6095–6103 (2021).
48. W. Woelffel *et al.*, Analysis of soda-lime glasses using non-negative matrix factor deconvolution of Raman spectra. *J. Non-Cryst. Solids* **428**, 121–131 (2015).
49. S. Hamad, C. E. Hughes, C. R. A. Catlow, K. D. M. Harris, Clustering of glycine molecules in aqueous solution studied by molecular dynamics simulation. *J. Phys. Chem. B* **112**, 7280–7288 (2008).
50. M. Di Gioacchino, M. A. Ricci, S. Imberti, N. Holzmann, F. Bruni, Hydration and aggregation of a simple amino acid: The case of glycine. *J. Mol. Liq.* **301**, 112407 (2020).
51. N. E. R. Zimmermann, B. Vorselaars, D. Quigley, B. Peters, Nucleation of NaCl from aqueous solution: Critical sizes, ion-attachment kinetics, and rates. *J. Am. Chem. Soc.* **137**, 13352–13361 (2015).
52. N. E. R. Zimmermann *et al.*, NaCl nucleation from brine in seeded simulations: Sources of uncertainty in rate estimates. *J. Chem. Phys.* **148**, 222838 (2018).
53. H. Jiang, P. G. Debenedetti, A. Z. Panagiotopoulos, Communication: Nucleation rates of supersaturated aqueous NaCl using a polarizable force field. *J. Chem. Phys.* **149**, 141102 (2018).
54. B. D. Saksena, Raman spectrum and molecular association in formamide. *Proc. Indian Acad. Sci. Math. Sci.* **11**, 53–61 (1940).
55. S. E. M. Colaianni, O. F. Nielsen, Low-frequency Raman spectroscopy. *J. Mol. Struct.* **347**, 267–283 (1995).
56. A. Datta, A. Hossain, Solubility data of glycine in water and justification of literature results. *Asian J. Chem.* **32**, 1525–1533 (2020).
57. T. Wilson, Resolution and optical sectioning in the confocal microscope. *J. Microsc.* **244**, 113–121 (2011).
58. K. Yuyama, T. Sugiyama, H. Masuhara, Millimeter-scale dense liquid droplet formation and crystallization in glycine solution induced by photon pressure. *J. Phys. Chem. Lett.* **1**, 1321–1325 (2010).
59. F. Pedregosa *et al.*, Scikit-learn: Machine learning in Python. *J. Mach. Learn. Res.* **12**, 2825–2830 (2011).
60. A. Esser, S. Belsare, D. Marx, T. Head-Gordon, Mode specific THz spectra of solvated amino acids using the AMOEBA polarizable force field. *Phys. Chem. Chem. Phys.* **19**, 5579–5590 (2017).
61. P. Eastman *et al.*, OpenMM 7: Rapid development of high performance algorithms for molecular dynamics. *PLOS Comput. Biol.* **13**, e1005659 (2017).
62. M. J. Frisch *et al.*, Gaussian 16, Revision C.01 (Gaussian, Inc., Wallingford, CT, 2016).